PHYSICAL REVIEW A **106**, 053527 (2022)

Thermodynamic and nonlinear optical analysis of solid-state multipass cells for compression of picosecond pulses in the 2-μm range

Chao Mei ,[1,*] Uwe Griebner,[2] and Günter Steinmeyer [2,3]

[1]*Research Center for Convergence Networks and Ubiquitous Services, SCCE,*
University of Science and Technology Beijing, Xueyuan Rd. 30, 100083 Beijing, China
[2]*Max Born Institute for Nonlinear Optics and Short Pulse Spectroscopy, Max-Born-Straße 2a, 12489 Berlin, Germany*
[3]*Institut für Physik, Humboldt Universität zu Berlin, Newtonstraße 15, 12489 Berlin, Germany*

(Received 19 July 2022; accepted 28 October 2022; published 30 November 2022)

Multipass cells (MPCs) recently emerged as a new femtosecond pulse compression technique for lasers with high pulse energy. While most of the work focused on the compression of near-infrared laser systems so far, we address the case of holmium-based gain materials, which offer an enormous potential in terms of pulse energy, yet can only host a very narrow bandwidth in the 2-μm wavelength range. Compression into the few-cycle regime, therefore, requires at least a hundredfold spectral broadening. Specifically, we investigate the utility of four different solid-state materials in the MPC, namely, fused silica, sapphire, YAG, and diamond. Spectral broadening dynamics is numerically investigated using the $2D + 1$-unidirectional pulse propagation equation. To this end, we put particular emphasis on the thermal properties of the nonlinear optical material, which turn out as a critical issue above 2-μm wavelength. Solving the heat equation for each of the materials, we then estimate the maximum temperature at beam center. These considerations show that outside the near infrared, thermodynamic parameters of nonlinear optical materials become at least equally important as their optical properties. Among the four materials under test, in particular, diamond stands out as it combines highly favorable thermal properties with a large optical nonlinearity. Finally, a concomitant slow degradation of spatial coherence is monitored. Our findings provide an effective guideline for the design of high pulse-energy compressors at wavelengths of 2 μm and beyond.

DOI: 10.1103/PhysRevA.106.053527

I. INTRODUCTION

With the rapid advance of ultrafast laser technology, high-energy few-cycle pulses are becoming increasingly accessible. Traditionally, given their broadband laser gain, Ti:sapphire lasers have an edge here [1]. Yet the feat of a broadband emission inevitably comes with a limited energy storage capability, that is, a saturation fluence of only about 1 J/cm^2. To this end, rare-earth-doped materials are often announced as a much more capable alternative, offering less than ten times larger saturation fluence. For example, with only a slightly increased center wavelength, Yb-doped fiber lasers [2] and Yb:YAG thin-disk laser systems [3] therefore offer a substantial increase in terms of saturation fluence, but at the expense of gain bandwidth and pulse duration. Considering chirped-pulse amplification in these media, therefore, Yb-doped laser gain materials offer a substantial increase of pulse energies generated in a medium with given dimensions, yet with the caveat of concomitantly increased pulse durations. Recently, the interest of generating high-energy few-cycle pulses has increasingly shifted towards even longer wavelengths in the 2-μm range, using holmium- or thulium-doped materials. In this range, Ho:YLF sticks out, with demonstrated pulse energies of more than 50 mJ at kHz repetition rate [4]. However, given the rather narrow band amplification range of this material, gain-narrowing effects limit the pulse duration of these laser systems to about 2 ps, requiring hundredfold compression to reach the few-cycle range [5], therefore, even increasing the intrinsic dilemma between pulse duration and energy in amplified laser systems. Pertinent extreme compression ratios require substantially more sophisticated approaches than early Ti:sapphire-based few-cycle pulse generation [6–10]. All these active compression schemes rely on a combination of a nonlinear medium and dispersion compensation, yet employ different geometries. Among the proven approaches for pulse compression, hollow-fiber compressors can probably be considered the most successful technique [5–7,10–13], with dispersion compensation typically relying on chirped mirrors. Notably, more recent successful schemes often involved multiplate schemes [14,15] or multipass cells (MPCs) [16–18], which considerably increased the toolbox of few-cycle pulse compression. Typically, the MPC method is implemented by utilizing the nonlinearity of a noble gas, i.e., the nonlinearity is distributed over the entire cavity, similar to the hollow-fiber approach. While this approach is certainly best suited for elevated pulse energies, using a solid-state nonlinear medium offers a much quicker accumulation of sufficient B integrals at somewhat lower pulse energies. To this end, the use of solid-state media rather than noble gases is appealing. So far, technical implementations of this scheme typically

---

[*] chaomei@ustb.edu.cn

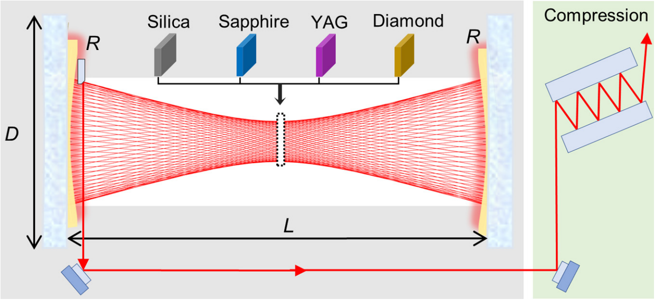

FIG. 1. The structure of solid-state MPC used for high-energy picosecond pulse compression in the 2-μm range. In the following, we assume that ideal dispersion compensation can be accomplished by a set of chirped mirrors, as indicated by the compression stage.

employed a single isolated dielectric slab within the focus of the multipass cell rather than using a continuous gaseous medium. In the following, we will refer to this particular geometry as solid-state MPC [16,18]. They exclusively operated around 1 μm with one exception at 1.5 μm [19]. All of them contained fused silica plates as a nonlinear medium and the compressed pulse energy is below 100 μJ [18]. The choice of a suitable nonlinear medium appears straightforward in the 1-μm range, with the rather proven choices of either sapphire or YAG [20–22]. Both of these materials excel with their thermal conductivity properties rather than only displaying superior nonlinear optical properties. To avoid multiphoton absorption (MPA) and ionization processes to the extent possible, materials with the largest band gap like LiF, CaF_2, or MgF_2 should be strongly preferred [23–25], which are nevertheless often found disappointing in terms of spectral broadening. Therefore, the key issue of the fluorides appears to be their low thermal conductivity and the rather low nonlinear refractive index that is intimately coupled to their large band gap. In the following, we revisit the scenario of a solid-state nonlinear medium inside a MPC, including the MPA processes, thermal conductivity, and linear absorption at 2-μm wavelength.

In the following we numerically study solid-state MPCs for the compression of 2-μm high-energy picosecond pulses. The energy, full width at half maximum (FWHM) duration, and center wavelength of the input pulse are set as 45 mJ, 3 ps, and 2.05 μm, respectively. These values are chosen according to our previous experimental data [4]. To explore the best-suited solid nonlinear medium that can be used for effective pulse compression in this wavelength range, four solid-state materials are considered, i.e., fused silica, sapphire, YAG, and diamond [26–29]. While sapphire and YAG were frequently used in the 1-μm range, we include fused silica for comparison as it exhibits relatively poor thermal properties in comparison to the crystalline materials. Diamond, on the other hand, shows the best thermal conductivity of all transparent dielectrics. As part of the pulse energy is absorbed and converted into heat during the compression process, we couple the nonlinear optical model to a thermodynamic analysis. The structure of solid-state MPCs to be studied in this work is shown in Fig. 1. The four different media are illustrated by different colors and assumed to be inserted into the center of the MPC under near-normal incidence. For practical purposes, the slab needs to be antireflection coated or Brewster-angled. The latter would then require additional compensation measures for astigmatism [30] and is not considered here. Parameters D and L describe the height and length of the designed solid-state MPC, respectively, and R is the radius of the curvature of the concave mirrors. The MPC is designed as a Herriott cell by adjusting L to satisfy the condition of $R < L < 2L$. The radius of the beam waist w_0 as well as the beam size on concave mirrors is calculated by the ABCD matrix formalism once the MPC structure is selected [17]. We assume that the concave mirrors are highly reflective $R = 99\%$. In the following sections, the theoretical framework and simulation results are described in detail.

II. THEORETICAL FRAMEWORK

The space-time nonlinear dynamics of pulse propagation in MPCs can be described by the unidirectional pulse propagation equation (UPPE) [31]. To simplify the calculation, we reduce the spatial coordinates from $3D + 1$ to $2D + 1$, using cyclindrical coordinates to replace (x, y, z, t) with (r, z, t). When space-time coupling [32] can be neglected, a $1D + 1$ model may also suffice to describe the nonlinear propagation in MPCs [33]. However, space-time coupling may play a role in this work due to high pulse energies and the thermodynamic analysis critically relies on the exact two-dimensional (2D) intensity distributions for reliably computing the resulting temperature fields. Therefore, the $2D + 1$ model is most suitable for this work. Mathematically, the $2D + 1$ UPPE is written as

$$\partial_z \widetilde{\mathcal{E}}_{k_\perp}(\omega, z) = ik_z \widetilde{\mathcal{E}}_{k_\perp}(\omega, z) + \frac{i\omega^2}{2\epsilon_0 c^2 k_z} \widetilde{\mathcal{P}}_\perp(\omega, z) - \frac{\omega}{2\epsilon_0 c^2 k_z} \widetilde{\mathcal{J}}_\perp(\omega, z), \tag{1}$$

where z is the propagation coordinate, $k_z = \sqrt{k^2(\omega) - k_\perp^2}$ is the z component of the wave vector k, where $k(\omega) = n(\omega)\omega/c$, ω is the angular frequency, c is the light speed in a vacuum, ϵ_0 is the permittivity in free space, and $n(\omega)$ is the complex linear refractive index, including both the refractive index $\bar{n}$ and linear losses by $n(\omega) = \bar{n}(\omega) + ik_e(\omega)$. Here k_e is the extinction ratio, which is proportional to the linear loss of the medium. Different from previous work, the linear loss must be considered here because all four solid materials under consideration show intrinsic absorption. To solve the UPPE efficiently, one needs to rewrite it in spectral representation. Actually, only the spectral amplitude $\widetilde{A}$, which is related to $\widetilde{\mathcal{E}}$ via $\widetilde{\mathcal{E}}_{k_\perp}(\omega, z) = \widetilde{A}_{k_\perp}(\omega, z)(ik_z z)$, enters into the nonlinear part. In Eq. (1), $\widetilde{\mathcal{P}}_\perp(\omega, z)$ is the nonlinear polarization term including both the instantaneous nonlinear refraction and the noninstantaneous Raman effect. In the time domain, the $\widetilde{\mathcal{P}}_\perp(\omega, z)$ can be written as

$$\mathcal{P}_\perp(t) = 2\epsilon_0 n_0 n_2 \left[(1 - f_R) I(t) + f_R \int_0^\infty \mathcal{R}(\tau) I(t - \tau) d\tau \right], \tag{2}$$

where $n_0 = \bar{n}(\omega_0)$ denotes the real part of $n(\omega)$ at pumping frequency ω_0, n_2 is the nonlinear refractive index of the employed solid plate whose frequency dependence is neglected,

TABLE I. Optical parameters for the four materials under test. n_0, GVD, k_e, and n_2: linear refractive, group-velocity dispersion, extinction ratio, and nonlinear refractive index at pump wavelength, respectively. f_R: fractional contribution of the Raman response. t_r: reciprocal of the single vibrational angular frequency. t_d: vibration damping time. τ_c: average collision time of electrons. τ_r: recombination time of free carriers. U_i: band gap. N: photon number. ρ_{nt}: density of neutral atoms.

Para. Mat.	n_0	GVD ($\mathrm{fs}^2/\mathrm{mm}$)	k_e $\times 10^{-7}$	n_2 (cm^2/W) $\times 10^{-16}$	f_R	t_r (fs)	t_d (fs)	τ_c (fs)	τ_r (fs)	U_i (eV)	N	ρ_nt (cm^{-3}) $\times 10^{22}$	Refs.
Silica	1.44	−113	2	1.94	0.18	12.5	32	20	150	7.8	13	2.1	[39–44]
Sapphire	1.74	25	13	2.44	0.25	200	182	1.7	96	9.9	17	2.4	[26,40,45–47]
YAG	1.8	−71	27	7	0.15	10	0.02	3	1000	6.5	11	7	[45,48–51]
Diamond	2.4	64	1.2	13	0.28	5700	4	3.6×10^8	–	5.5	10	18	[29,52–56]

$I(t)$ denotes the intensity of propagating pulse, f_R stands for the fractional contribution of the Raman response, and $\mathcal{R}(t)$ represents a memory function that describes the Raman effect. The $\mathcal{R}(t)$ for four materials can be generally expressed in an unified form as [34]

$$\mathcal{R}(t) = \left(t_r^{-2} + t_d^{-2}\right) t_r \exp(-t/t_d) \sin(t/t_r), \tag{3}$$

where t_r is the reciprocal of the single vibrational angular frequency and t_d is the vibration damping time. Values for t_r and t_d are listed in Table I.

The plasma-induced current $\mathcal{J}$ accounts for the average dissipated power that is caused by optical ionization. The time-dependent differential equation for $\mathcal{J}$ is given as [34]

$$\frac{\partial \mathcal{J}}{\partial t} + \frac{\mathcal{J}}{\tau_c} = \frac{q_e^2}{m_e} \rho_e \mathcal{E}, \tag{4}$$

in which ρ_e represents the electron density, τ_c is the average collision time of electrons, q_e is the elementary charge, and m_e is the reduced electron-hole mass. While the real part of $\mathcal{J}$ accounts for plasma absorption, its imaginary part allows for the plasma defocusing. The charge density $\rho(r,t)$ itself is governed by another rate equation with additional attenuation term [34]

$$\frac{\partial \rho_e}{\partial t} = W_{\mathrm{MP}}(I)(\rho_{\mathrm{nt}} - \rho) + W_{\mathrm{ava}}(I)\rho_e - \rho_e/\tau_r, \tag{5}$$

where $W_{\mathrm{MP}} = \sigma_N I^N$ denotes the multiphoton ionization rate, σ_N is the respective cross section, and N the photon number defined by $N = \mathrm{mod}[U_i/(\hbar\omega_0)] + 1$. $\hbar$ is the reduced Planck constant and U_i is the band gap. It is obvious that N is determined by both the band gap of the material and the pump angular frequency. Finally, ρ_{nt} represents the density of neutral atoms, $W_{\mathrm{ava}} = \sigma(\omega_0)I/U_i$ is the rate of avalanche ionization proportional to the light intensity, and τ_r is the recombination time of free carriers. We emphasize that free-carrier recombination must be taken into account in this work because the picosecond input pulse duration can be an order of magnitude larger than τ_r, cf. Table I. Shielding against potential catastrophic damage issues, we apply the criterion of [35], demanding that the resulting partial ionization stay below 0.1%. The avalanche ionization coefficient $\sigma(\omega_0)$ at ω_0 is written as [34]

$$\sigma(\omega_0) = \frac{\omega_0^2 \tau_c}{n_0 c \rho_c} \frac{1 + i\omega_0\tau_c}{1 + \omega_0^2\tau_c^2}, \tag{6}$$

where $\rho_c = \epsilon_0 m_e \omega_0^2/q_e^2$ is the critical plasma density. For a comprehensive presentation of the optical properties for the four materials employed, we summarize their parameters in Table I. It should be noted that, according to its collision time, τ_c of diamond is estimated to be on the order of nanoseconds. Therefore, the free-carrier recombination can be neglected in this particular case. Moreover, the value for k_e of YAG in Table I is a fitted value.

The input pulse is assumed with Gaussian temporal and spatial profile at $z = 0$ according to

$$\mathcal{E}(r, t, z = 0) = \sqrt{I_{\mathrm{in}}} \exp\left[-\frac{r^2}{w_0^2} - \frac{t^2}{t_0^2} - ik_0\frac{r^2}{2f}\right], \tag{7}$$

where I_{in} is the input intensity and w_0 and t_0 denote the beam radius and the pulse width, respectively. Here w_0 is deliberately chosen as large as 500 μm to limit the buildup of an overcritical plasma density >0.1% [35]. The wave number is defined as $k_0 = 2\pi/\lambda_0$, where $\lambda_0 = 2.05$ μm is chosen as the center wavelength, according to the maximum gain wavelength of Ho:YLF [4]. The FWHM definition of pulse width t_F is connected to t_0 via $t_F = \sqrt{2\ln 2}t_0$. We further set t_F to 3 ps throughout because the rather strong gain-narrowing effects in Ho:YLF render it difficult to obtain significantly shorter pulses from regenerative amplifiers [36,37].

Using Eq. (1), we now compute the cumulated energy loss for the propagation inside the MPC. All dissipative effects inside the nonlinear medium lead to a highly localized temperature increase within the modal volume of the laser beam. This thermodynamic process is modeled by the transient heat equation [38]

$$\rho_m C_p \frac{\partial T(t, r, z)}{\partial t} + \nabla \cdot [-K\nabla T(t, r, z)] = Q(r, z), \tag{8}$$

where ρ_m is the mass density of the medium, C_p the specific heat capacity, K the thermal conductivity, $T(t, r, z)$ the $2D + 1$ temperature field, and $Q(r, z)$ the heat source. The heat source Q is given by the absorbed intensity I_{ab} of propagating pulses according to $Q(r, z) = \int_{-\infty}^{\infty} I_{\mathrm{ab}}(r, t, z)dt/\Delta z$, where Δz is the step size along the axial dimension Here we already neglect any time dependence of the heat source as diffusive defects are slow compared to both the picosecond timescales of the laser pulses and the typical few-kHz repetition rates under consideration. Moreover, as we are considering a solid medium, convective heat transfer is neglected in Eq. (8). Nevertheless, convective and radiative cooling have to be considered at the front and rear surfaces of the nonlinear medium. These cooling processes are included as Neumann boundary conditions, with convective and radiative loss rates $\Gamma_{\mathrm{conv}} = h\Delta[T(r, z \in \{0, d = 1\,\mathrm{mm}\}) - T_{\mathrm{amb}}]$ and $\Gamma_{\mathrm{rad}} = \epsilon\sigma[T^4(r, z \in \{0, d = 1\,\mathrm{mm}\}) - T^4_{\mathrm{amb}}]$, respectively. Here $\sigma = 5.67 \times 10^{-8}\ \mathrm{W/(m^2\ K^4)}$ is the Stefan-Boltzmann constant, ϵ the emissivity of the material, which is estimated as $\epsilon = 0.7$ throughout. The heat-transfer coefficient h was assumed as 50, i.e., slightly below the possible onset of a turbulent air flow. This assumption corresponds to maximum convective cooling at the optical surfaces. Then we consider the Dirichlet boundary condition $T(r_0 = 1.5\,\mathrm{mm}) = T_{\mathrm{amb}} = 20\,^{\circ}\mathrm{C}$ for the nonoptical cylindrical surface, i.e., we assume that the optical medium is clamped to a heat sink at constant ambient temperature at its perimeter. It is worth noting that convective and radiative cooling only play a minor role here, in particular in the simulation of crystalline optical media with their rather high thermal conductivities. Equation (8) can now be integrated out over time to yield the steady-state heat equation for determining the static solution $T(r, z)$

$$\nabla \cdot [-K\nabla T(r, z)] = Q(r, z). \tag{9}$$

Now the resulting temperature profile is only determined by two parameters, namely the thermal conductivity K and the source term $Q(r, z)$. The source term will now only be derived from the pulse propagation simulation runs, accounting for both linear contributions and those resulting from multiphoton processes. In the following, we will first analyze the properties of the compressed optical pulses with the aim of obtaining the shortest possible pulses and widest spectra in the MPC. This will then be followed by a discussion of the resulting temperature profiles using the above thermodynamic analysis.

III. SIMULATION RESULTS

We start our discussion of the simulation results with an analysis of pulse compression in four cylindrical solid plates of different materials. To simplify the comparison, we assume identical thickness of $d = 1$ mm and radius of $r_0 = 1.5$ mm, i.e., we clip the beam at three times its waist radius of $w_0 = 0.5$ mm. This choice is probably the tightest practical diameter of the nonlinear medium, maximizing the cooling potential at the cylindrical surface used for heat sinking. We further assume identical conditions for the input pulse, i.e., $t_{\mathrm{F}} = 3\,\mathrm{ps}$ and 45 mJ pulse energy for all materials. At the identical pump wavelength of 2.05 μm, the group-velocity dispersion (GVD) of fused silica, sapphire, YAG, and diamond are shown in Table I. Figure 2 shows the compression factor F and the energy efficiency η versus number of passes on the left and right vertical axes, respectively. F is defined as the ratio between the output and input pulse width and the corresponding efficiency η is defined as the ratio between output and input energy, characterizing pulse compression and energy loss, respectively. For the calculation of F, we assume optimum dispersion compensation, i.e., we effectively compute the Fourier transform of the broadened spectra here to show the maximum compression potential obtainable from the respective MPC. The efficiency calculation only accounts for linear and nonlinear losses inside the material as well as for dissipative effects due to clipping at $r = r_0$, but not for Fresnel losses due to imperfections of antireflection coatings.

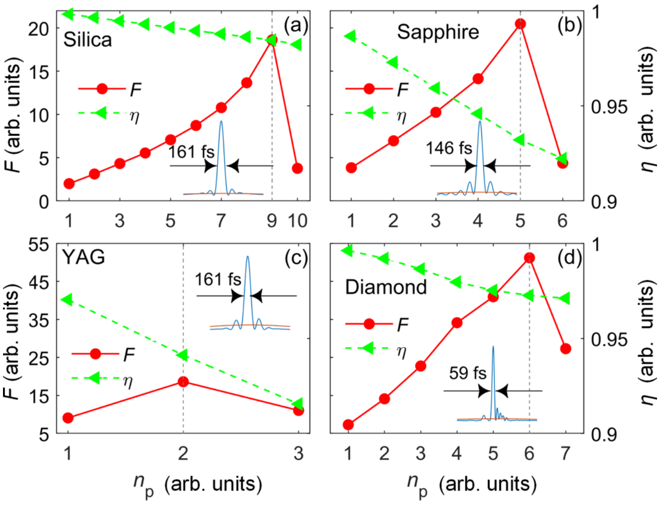

FIG. 2. Variation of compression factor F and energy efficiency η vs. number of passes n_p for MPCs using (a) fused silica, (b) sapphire, (c) YAG and (d) diamond plates inside the focal position of the cavity. Insets show corresponding temporal waveforms for input (red) and output (blue) pulses.

Depending on the material, optimum compression is reached after two to nine passes, with a maximum value $F > 50$ for diamond. This unexpectedly high compression factor enables direct compression of 3 ps pulses down to sub-60-fs pulse duration in a single compression stage and is accompanied by an efficiency of 97%. The latter value is only exceeded using fused silica as the nonlinear medium whereas the crystalline materials sapphire and YAG perform substantially poorer in terms of efficiency. Compression factors for fused silica, sapphire, and YAG are all in the range of 20, allowing direct compression down to about 150 to 160-fs duration.

To better understand the dynamics of F evolution, we introduce the B integral [57], which measures the accumulation of the nonlinear phase caused by self-phase modulation

$$B_{\mathrm{int}} = \frac{2\pi n_2}{\lambda} \int_0^d \frac{P_{\mathrm{peak}}(z)}{A_{\mathrm{eff}}(z)} dz, \tag{10}$$

where $P_{\mathrm{peak}}(z)$ is the localized peak power and $A_{\mathrm{eff}}(z)$ is the localized effective mode area at propagation distance z. As silica and YAG exhibit negative GVD in the 2-μm region, soliton-like self-compression effects may appear and lead to an increase of $P_{\mathrm{peak}}(z)$. A much stronger contribution to increasing the B integral is expected from self-focusing effects, which may lead to a catastrophic optical collapse that has to be absolutely avoided lest optical damage occur. Prior to the onset of damage, one often observes plasma-induced defocusing effects, which cause a pulse break-up in the temporal domain and the formation of ring-like structures in the radial domain. Figure 3 shows computed cross sections through the r-λ domain for the situation of maximum compression in Fig. 2. Calculating the B integral from Eq. (10), we arrive at an estimate of $B \approx 8.7\pi$, 8.2π, and 7.7π for the case of silica, sapphire, and YAG, respectively. These numbers are consistent with the observed maximum 20-fold spectral broadening and possible compression in Fig. 2. In contrast, diamond leads to much higher values of $B \approx 24.2\pi$, and at least the onset of

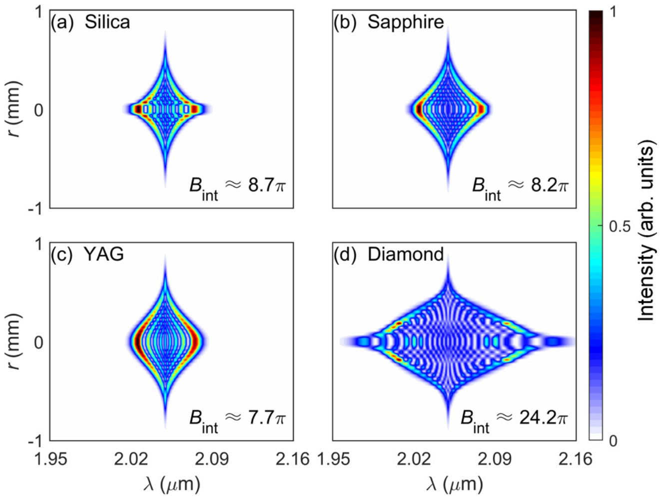

FIG. 3. Spatiospectral intensity distribution for (a) fused silica, (b) sapphire, (c) YAG, and (d) diamond when F reaches its maximum. The corresponding B integrals are calculated for four employed materials.

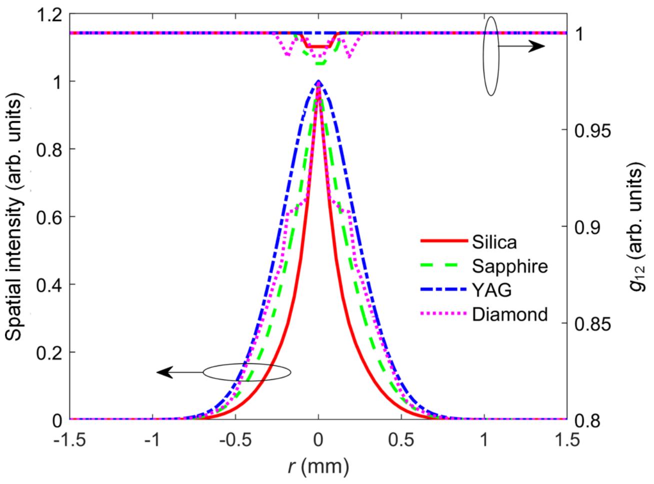

FIG. 4. The distribution of spatial intensity $I(r)$ (left) and spatial coherence g_{12} (right) over r when F reaches its maximum for silica (red solid curve), sapphire (dashed green curve), YAG (dashed dotted blue curve), and diamond (dotted magenta curve).

the formation of a radial ring structure can be seen near 2.01- and 2.10-μm wavelength. Nevertheless, these effects can still be considered as rather mild, leading to the reduction of beam quality rather than any catastrophic consequences.

To scrutinize any possible concomitant degradation of spatial coherence during nonlinear propagation, we introduce the first-order coherence g_{12} [58,59], which is defined as

$$g_{12}(r) = \left| \frac{\langle \hat{\mathcal{E}}_m(r)\hat{\mathcal{E}}_n^*(r)\rangle_{m\neq n}}{\sqrt{\langle|\hat{\mathcal{E}}_m(r)|^2\rangle\langle|\hat{\mathcal{E}}_n^*(r)|^2\rangle}} \right|, \tag{11}$$

where the angular brackets represent an average over nonidentical pairs of optical fields, which are indexed by m and n. Here $\hat{\mathcal{E}}_n(r) = \int_{-\infty}^{\infty} \mathcal{E}_n(r,t)dt$ is the complex-valued spatial amplitude after time-domain integration. Spatial pulse pairs are obtained from an ensemble of 50 simulation runs with independent noise fields seeded by one photon per mode [60]. At a given spatial position r, $0 \leqslant g_{12}(r) \leqslant 1$ where $g_{12}(r) \approx 1$ indicates excellent stability in amplitude and phase. Calculated g_{12} values versus radius are shown in Fig. 4 for the situation of maximum F. In addition, we also illustrate the resulting integrated radial beam profiles within the nonlinear medium. Near $r = 0$, the spatial coherence g_{12} generally degrades to a value near 0.97 for all materials but YAG. The coherence degradation at beam center is accompanied by deviations from the initial Gaussian profile. This transfer of energy into higher-order spatial modes is most pronounced for diamond, where coherence is additionally degraded off-center and a pronounced shoulder appears near $r = 0.2$ mm. In some sense, this pedestal structure can be understood as the spatial analog of the infamous coherent artifact in temporal pulse characterization [61,62].

At this point of the discussion, one would conclude that both fused silica and sapphire appear to be valid choices, showing good spectral broadening at relatively high efficiencies. YAG appears to exhibit efficiency issues while diamond shows some indications for an immediate spatial beam breakup. Yet this premature conclusion does not take into account thermal effects. While to some extent such effects can be compensated by suitable adjustment of the MPC, a limit is reached when the focal length associated with thermal lensing effects reaches the dimension of the cavity.

To analyze the detrimental thermal lensing effects, we compute the absorbed energy $E_{\mathrm{in}} - E(z)$ as a function of t. Calculation results for $E(z)$ are shown in Fig. 5. In these simulations, we switched off individual dissipative mechanisms to trace the origin of the observed losses in Fig. 2. As one can see in Figs. 5(a) to 5(c), linear absorption nearly exclusively contributes to the losses for silica, sapphire, and YAG, i.e., switching off MPA or plasma avalanche effects

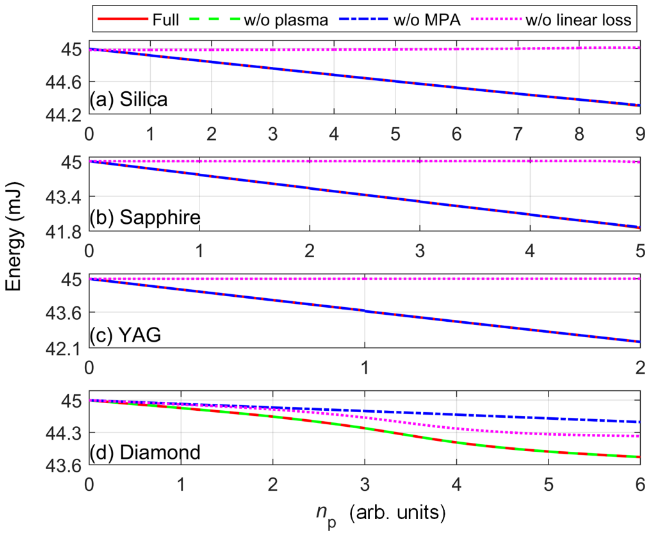

FIG. 5. The variation of pulse energy with n_p for (a) silica, (b) sapphire, (c) YAG, and (d) diamond. The pulse energy under full model (solid red curve), without plasma (dashed green curve), with MPA (dashed dotted blue curve), and without linear loss (dotted magenta curve) are calculated.

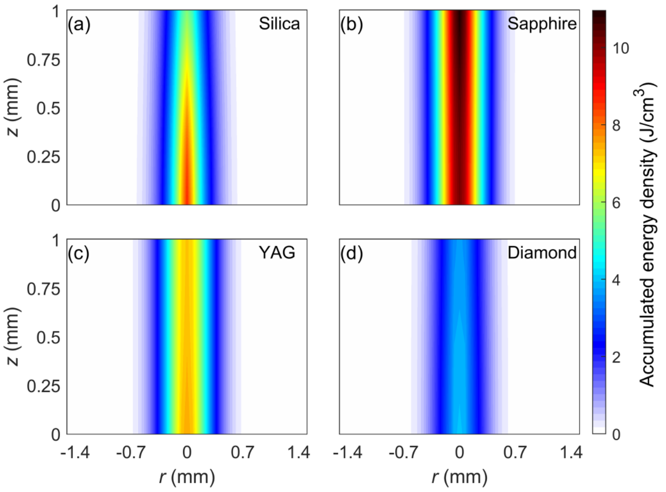

FIG. 6. The spatial distribution of accumulated energy density inside solid-state slab when F reaches its maximum for (a) silica, (b) sapphire, (c) YAG and (d) diamond.

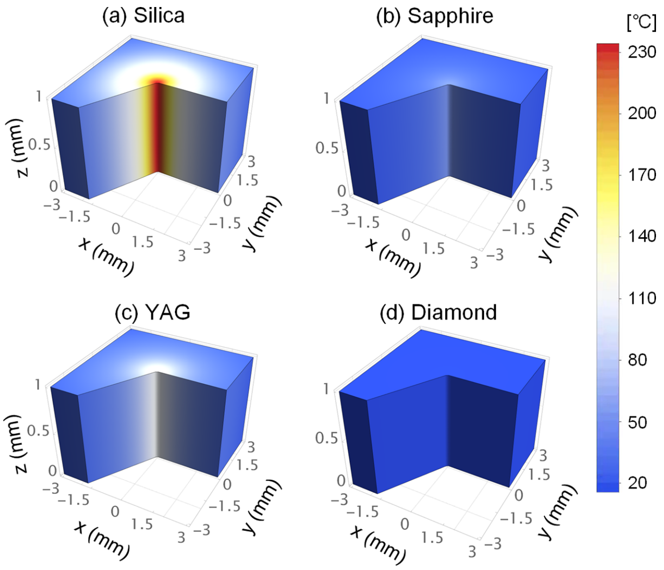

FIG. 7. Three-dimensional view of the temperature distribution over entire plate when F reaches its maximum for (a) silica, (b) sapphire, (c) YAG, and (d) diamond.

does not result in any significant change of pulse energy. Therefore, linear losses are solely responsible for dissipative effects in silica, sapphire, and YAG and amount to 0.69, 3.01, and 2.65 mJ, respectively. Accounting for the n_p through the nonlinear medium, this corresponds energy attenuation rates of 0.08, 0.60, and 1.33 mJ/mm, respectively. This information together with the corresponding k_e are also included in Table I. The dominant linear absorption is contrasted by the behavior of diamond, where MPA clearly dominates. Specifically, MPA causes a 0.78-mJ energy loss in diamond and linear losses consume only 0.47 mJ. These dominant nonlinear losses are explained by the rather small band gap of diamond of only 5.5 eV. It is nevertheless striking that the resulting total absorption remains smaller than for sapphire and YAG and that avalanche processes do not appear to play any role yet.

As a final aspect of our study, we find it instructive to study the spatial distribution of the absorbed energy inside a solid plate. We therefore construct a parameter V_{AE} that describes the spatial distribution of energy density integrated over multiple passes until F reaches maximum value. We write this parameter as

$$V_{\mathrm{AE}}(r,z)=\frac{1}{\Delta z}\sum_{n_p=1}^{N_p} I_r^{\mathrm{int}}(r,z,n_p)\frac{\Delta E_i(z,n_p)}{E_i(z,n_p)}, \tag{12}$$

where $\Delta z = z_i - z_{i-1}$ is again the longitudinal step size and i is the step number, $I_r^{\mathrm{int}}(r,z,n_p)=\int_{-\infty}^{\infty} I(r,t,z,n_p)dt$ is the integrated intensity over t, $\Delta E_i(z,n_p)=E_{i-1}(z,n_p)-E_i(z,n_p)$ is the energy difference that the pulse experiences when it propagates one axial step from z_{i-1} to z_i, i.e., the absorbed energy during one Δz. It can be seen from Eq. (12) that $V_{\mathrm{AE}}(r,z)$ is a superimposed energy density over n_p. For silica, sapphire, YAG, and diamond, the corresponding N_p are 9, 5, 2, and 6, respectively. The spatial distributions of $V_{\mathrm{AE}}(r,z)$ are shown in Fig. 6. From Fig. 6(a) we can see that the superposed $V_{\mathrm{AE}}(r,z)$ near the front facet (z = 0–0.5 mm) is larger than that at the rear. At first glance, this scenario appears contrary to our expectation that self-focusing effects should occur during the second half of propagation. However, taking into account the round-trip propagation of the beam inside the MPC, this picture seems reasonable because, for an even n_p, the propagation direction is reverted and self-focusing dominates near $z = 0$. A pronounced unbalanced propagation phenomenon appears for silica. Figure 6 is also instructive to understand the difference to thermal lensing effects in traditional lamp-pumped solid state lasers [63], where it is usually assumed that dissipative effects are homogeneous. In the MPC, in contrast, heating effects are highly localized and confined to a diameter in the range from 20 μm (silica) to 50 μm (diamond). It is therefore not immediately clear whether we can use the theoretical treatment in Ref. [63] to estimate the resulting focal length f_θ of the thermal lensing effect.

To address this problem, we numerically solve Eq. (9). We assume a repetition rate $f_{\mathrm{rep}} = 1$ kHz and an ambient temperature of 20 °C. The simulation results are shown in Fig. 7. While it can be seen that for all materials, temperatures on axis are much higher than those at the perimeter, deviations from the analytical solution of the heat equation remain rather small. However, resulting on-axis temperatures can be as high as 255 °C in silica [Fig. 7(a)] whereas diamond exhibits a nearly vanishing heating effect of only 0.3 °C [Fig. 6(d)] due to its extremely high heat conductivity. Peak temperatures for all four materials are compiled in Table II. Maximum temperatures in Table II have to be considered absolute maximum values, as dictated either by melting, disintegration, or oxidization under atmospheric conditions [64,65]. In particular, for materials with low thermal conductivity, thermal stress may cause catastrophic optical damage at much lower temperatures. We therefore consider a local temperature maximum of 300 °C as a more practical safe limit. While it appears obvious that fused silica is unsuitable for an MPC operated at 2-μm wavelength, we estimated the order of magnitude of the thermal focal length f_θ from the temperature dependence

TABLE II. Thermodynamic parameters for four materials [63,66,67]. Max. temp.: absolute maximum temperature when either melting or disintegration occurs [68]; Peak temp.: calculated temperature at beam center.

Para. \ Mat.	Silica	Sapphire	YAG	Diamond
K (W m^{-1} K^{-1})	1.42	40	14	3000
$dn/dT\,(10^{-6}\text{K}^{-1})$	11.5	12	7.3	7.7
Max. temp. (°C)	1000	1600	1700	750
Peak temp. (°C)	255	58	110	20.3
f_θ(m)	1.9	15	10	4000

of the refractive index

$$f_\theta = \frac{2K\pi r_0^2}{(1-\eta)E_{\text{in}}f_{\text{rep}}}\left(\frac{dn}{dT}\right)^{-1}. \tag{13}$$

Values for the temperature coefficient of the refractive index are included in Table II for all four materials [63,66,67]. This simplified treatment neglects stress-induced effects, which are expected to further decrease f_θ by ≈25% for YAG [63]. We also neglect the end cap effect, even though it probably plays a stronger role in our disk-shaped media than in elongated laser rods. Accounting only for thermal refraction effects, we compute $f_\theta < 2$ m for fused silica, which clearly confirms our concerns on the poor suitability of this material for compression of high-energy laser pulses at 2 μm. In YAG and sapphire, thermal lensing effects are markedly weaker [cf. Table II], but require energy-dependent adjustments of the cavity design to adapt thermal lenses in the 10-m range. In contrast, f_θ remains in the kilometer range for diamond. Thermal focal lengths $f_\theta \geqslant 10$ m are large compared to typical dimensions of MPCs. With the noted exception of fused silica, detrimental thermal lensing effects can therefore be compensated by suitable alignment.

IV. CONCLUSION

In conclusion, we find that the compression of multi-mJ pulse energies at wavelengths of 2 μm and above does not necessarily have to resort to gaseous nonlinear media. So far, noble gases have been typically used for this purpose either in MPCs or hollow fiber compressors because they do not exhibit any absorption in the entire infrared range up to arbitrarily large wavelengths. However, this feat comes with two potential caveats. First, the Kerr nonlinearity of noble gases is rather low [69], which either requires tight focusing or a large number of passes in a MPC. Second, and different from the solid media, highly localized heating due to MPA in a MPC can lead to the onset of atmospheric turbulence inside the gas [70]. Hollow-fiber compressors, on the other hand, are limited in their capability to host pulse energies much above 10 mJ [10], which require large inner capillary diameters and, in turn, lengths of several meters to produce sufficient B integrals. Using solid-state materials inside an MPC is not an obvious alternative, as essentially all wide-band-gap solid-state exhibit a certain amount of losses above 2-μm wavelength. In many materials these losses are due to the presence of OH contaminations, but even in homonuclear materials like diamond, multiphonon absorption effects induce nonnegligible losses above 2.5-μm wavelength. As absorption is virtually unavoidable in solid-state dielectrics, thermal conductivity plays the most important role in the choice of the material, and this clearly favors diamond with its excellent thermal properties. Another interesting candidate may be silicon carbide, which exhibits an even higher nonlinearity, but significantly lower band gap and about ten times lower heat conductivity and is birefringent. As one could already see, the onset of detrimental effects on the beam profile in diamond with its ≈1 eV larger band gap, we therefore do not expect that SiC will outperform diamond.

Summarizing this discussion, it appears of paramount importance to choose nonlinear optical materials that combine favorable nonlinear optical and thermal properties in solid-state MPC compression schemes, in particular, when dissipative effects are virtually unavoidable. Moreover, in the infrared region above 2-μm wavelength, traditional criteria as a wide band gap can be mitigated to some extent. Rather, thermal conductivity takes the lead role for selecting a suitable material. This surprising shift of focus may lead to more efficient pulse compression schemes in the midinfrared, which surpass traditional hollow-fiber compression both in terms of pulse energy and compression factors. Given the high utility of long wave-based high-harmonic generation due to their large ponderomotive energy, our findings open an avenue for previously unprecedented applications of immediate mid-IR laser sources.

ACKNOWLEDGMENTS

This work was supported by the National Natural Science Foundation of China (Grant No. 62205015), the Guangdong Basic and Applied Basic Research Foundation (Grant No. 2021A1515110507), and the Fundamental Research Funds for the central universities (Grants No. 00007475 and No. QNXM20220042).

---

[1] A. Trisorio, P. M. Paul, F. Ple, C. Ruchert, C. Vicario, and C. P. Hauri, Ultrabroadband TW-class Ti:sapphire laser system with adjustable central wavelength, bandwidth and multi-color operation, Opt. Express **19**, 20128 (2011).

[2] P. Wan, L.-M. Yang, and J. Liu, All fiber-based Yb-doped high energy, high power femtosecond fiber lasers, Opt. Express **21**, 29854 (2013).

[3] T. Nubbemeyer, M. Kaumanns, M. Ueffing, M. Gorjan, A. Alismail, H. Fattahi, J. Brons, O. Pronin, H. G. Barros, Z. Major, T. Metzger, D. Sutter, and F. Krausz, 1 kW, 200 mJ picosecond thin-disk laser system, Opt. Lett. **42**, 1381 (2017).

[4] L. von Grafenstein, M. Bock, D. Ueberschaer, A. Koç, U. Griebner, and T. Elsaesser, 2.05 μm chirped pulse amplification

system at a 1 kHz repetition rate 2.4 ps pulses with 17 GW peak power, Opt. Lett. **45**, 3836 (2020).

[5] T. Nagy, L. von Grafenstein, D. Ueberschaer, and U. Griebner, Femtosecond multi-10-mJ pulses at 2 μm wavelength by compression in a hollow-core fiber, Opt. Lett. **46**, 3033 (2021).

[6] M. Nisoli, S. De Silvestri, O. Svelto, R. Szipöcs, K. Ferencz, C. Spielmann, S. Sartania, and F. Krausz, Compression of high-energy laser pulses below 5 fs, Opt. Lett. **22**, 522 (1997).

[7] T. Nagy, S. Hädrich, P. Simon, A. Blumenstein, N. Walther, R. Klas, J. Buldt, H. Stark, S. Breitkopf, P. Jójárt, I. Seres, Z. Várallyay, T. Eidam, and J. Limpert, Generation of three-cycle multi-millijoule laser pulses at 318 W average power, Optica **6**, 1423 (2019).

[8] J. I. Kim, Y. G. Kim, J. M. Yang, J. W. Yoon, J. H. Sung, S. K. Lee, and C. H. Nam, Sub-10 fs pulse generation by post-compression for peak-power enhancement of a 100-TW Ti:sapphire laser, Opt. Express **30**, 8734 (2022).

[9] R. Safaei, O. Kwon, P. Lassonde, V. Cardin, E. Haddad, A. Leblanc, B. E. Schmidt, H. Ibrahim, and F. Légaré, Low energy pulse compression in hollow core fibers using hydrofluorocarbon molecular gas, OSA Continuum **2**, 1488 (2019).

[10] C. Mei, I. Babushkin, T. Nagy, and G. Steinmeyer, Spatial cage solitons—taming light bullets, Photon. Res. **10**, 148 (2022).

[11] G. Fan, P. A. Carpeggiani, Z. Tao, G. Coccia, R. Safaei, E. Kaksis, A. Pugzlys, F. Légaré, B. E. Schmidt, and A. Baltuška, 70 mJ nonlinear compression and scaling route for an Yb amplifier using large-core hollow fibers, Opt. Lett. **46**, 896 (2021).

[12] D. Schade, F. Köttig, J. R. Koehler, M. H. Frosz, P. S. Russell, and F. Tani, Scaling rules for high quality soliton self-compression in hollow-core fibers, Opt. Express **29**, 19147 (2021).

[13] T. Nagy, P. Simon, and L. Veisz, High-energy few-cycle pulses: post-compression techniques, Adv. Phys.: X **6**, 1845795 (2021).

[14] C.-L. Tsai, Y.-H. Tseng, A.-Y. Liang, M.-W. Lin, S.-D. Yang, and M.-C. Chen, Nonlinear compression of intense optical pulses at 1.55 μm by multiple plate continuum generation, J. Lightw. Technol. **37**, 5100 (2019).

[15] J. E. Beetar, S. Gholam-Mirzaei, and M. Chini, Spectral broadening and pulse compression of a 400 μJ, 20 W Yb:KGW laser using a multiplate medium, Appl. Phys. Lett. **112**, 051102 (2018).

[16] E. Vicentini, Y. Wang, D. Gatti, A. Gambetta, P. Laporta, G. Galzerano, K. Curtis, K. McEwan, C. R. Howle, and N. Coluccelli, Nonlinear pulse compression to 22 fs at 15.6 μJ by an all-solid-state multipass approach, Opt. Express **28**, 4541 (2020).

[17] C. Mei and G. Steinmeyer, Space-time focusing and coherence properties of supercontinua in multipass cells, Phys. Rev. Res. **3**, 013259 (2021).

[18] A.-L. Viotti, M. Seidel, E. Escoto, S. Rajhans, W. P. Leemans, I. Hartl, and C. M. Heyl, Multi-pass cells for post-compression of ultrashort laser pulses, Optica **9**, 197 (2022).

[19] G. Jargot, N. Daher, L. Lavenu, X. Delen, N. Forget, M. Hanna, and P. Georges, Self-compression in a multipass cell, Opt. Lett. **43**, 5643 (2018).

[20] A. Dharmadhikari, F. Rajgara, and D. Mathur, Systematic study of highly efficient white light generation in transparent materials using intense femtosecond laser pulses, Appl. Phys. B **80**, 61 (2005).

[21] M. Bradler, P. Baum, and E. Riedle, Femtosecond continuum generation in bulk laser host materials with sub-μJ pump pulses, Appl. Phys. B **97**, 561 (2009).

[22] A. Dubietis, G. Tamošauskas, R. Šuminas, V. Jukna, and A. Couairon, Ultrafast supercontinuum generation in bulk condensed media, Lith. J. Phys. **57**, 113 (2017).

[23] A. Brodeur and S. L. Chin, Ultrafast white-light continuum generation and self-focusing in transparent condensed media, J. Opt. Soc. Am. B **16**, 637 (1999).

[24] A. Brodeur and S. L. Chin, Band-Gap Dependence of the Ultrafast White-Light Continuum, Phys. Rev. Lett. **80**, 4406 (1998).

[25] M. Sheik-Bahae, D. Hutchings, D. Hagan, and E. Van Stryland, Dispersion of bound electron nonlinear refraction in solids, IEEE J. Quantum Electron. **27**, 1296 (1991).

[26] J. H. Kim, M.-K. Chen, C.-E. Yang, S. S. Y. Jon Lee, P. Ruffin, E. Edwards, C. Brantley, and C. Luo, Broadband IR supercontinuum generation using single crystal sapphire fibers, Opt. Express **16**, 4085 (2008).

[27] S. Cheng, G. Chatterjee, F. Tellkamp, A. Ruehl, and R. J. D. Miller, Multi-octave supercontinuum generation in YAG pumped by mid-infrared, multi-picosecond pulses, Opt. Lett. **43**, 4329 (2018).

[28] A. Shams-Ansari, P. Latawiec, Y. Okawachi, V. Venkataraman, M. Yu, B. Desiatov, H. Atikian, G. L. Harris, N. Picqué, A. L. Gaeta, and M. Lončar, Supercontinuum generation in angle-etched diamond waveguides, Opt. Express **44**, 4056 (2019).

[29] B. J. M. Hausmann, I. Bulu, V. Venkataraman, P. Deotare, and M. Lonar, Diamond nonlinear photonics, Nat. Photonics **8**, 369 (2014).

[30] J. B. McManus, P. L. Kebabian, and M. S. Zahniser, Astigmatic mirror multipass absorption cells long-pass-length spectroscopy, Appl. Opt. **34**, 3336 (1995).

[31] M. Kolesik, J. V. Moloney, and M. Mlejnek, Unidirectional Optical Pulse Propagation Equation, Phys. Rev. Lett. **89**, 283902 (2002).

[32] A. L. Gaeta, Catastrophic Collapse of Ultrashort Pulses, Phys. Rev. Lett. **84**, 3582 (2000).

[33] N. Daher, F. Guichard, S. W. Jolly, X. Delen, F. Quéré, M. Hanna, and P. Georges, Multipass cells: 1D numerical model and investigation of spatio-spectral couplings at high nonlinearity, J. Opt. Soc. Am. B **37**, 993 (2020).

[34] A. Couairon, E. Brambilla, T. Corti, D. Majus, O. de J. Ramírez-Góngora, and M. Kolesik, Practitioners guide to laser pulse propagation models and simulation, Eur. Phys. J.: Spec. Top. **199**, 5 (2011).

[35] M. Mero, J. Liu, W. Rudolph, D. Ristau, and K. Starke, Scaling laws of femtosecond laser pulse induced breakdown in oxide films, Phys. Rev. B **71**, 115109 (2005).

[36] P. Fuertjes, L. von Grafenstein, D. Ueberschaer, C. Mei, U. Griebner, and T. Elsaesser, Compact OPCPA system seeded by a Cr:ZnS laser for generating tunable femtosecond pulses in the MWIR, Opt. Lett. **46**, 1704 (2021).

[37] P. Fuertjes, L. von Grafenstein, C. Mei, M. Bock, U. Griebner, and T. Elsaesser, Cr:ZnS-based soliton self-frequency shifted signal generation for a tunable sub-100 fs MWIR OPCPA, Opt. Express **30**, 5142 (2022).

[38] J. H. Lienhard IV and J. H. Lienhard V, *A Heat Transfer Textbook*, 5th ed., (Dover, Mineola, NY, 2019)

[39] R. Kitamura, L. Pilon, and M. Jonasz, Optical constants of silica glass from extreme ultraviolet to far infrared at near room temperature, Appl. Opt. **46**, 8118 (2007).

[40] G. N. Patwardhan, J. S. Ginsberg, C. Y. Chen, M. M. Jadidi, and A. L. Gaeta, Nonlinear refractive index of solids in mid-infrared, Opt. Lett. **46**, 1824 (2021).

[41] K. Blow and D. Wood, Theoretical description of transient stimulated Raman scattering in optical fibers, IEEE J. Quan. Electron. **25**, 2665 (1989).

[42] R. H. Stolen, J. P. Gordon, W. J. Tomlinson, and H. A. Haus, Raman response function of silica-core fibers, J. Opt. Soc. Am. B **6**, 1159 (1989).

[43] L. Sudrie, A. Couairon, M. Franco, B. Lamouroux, B. Prade, S. Tzortzakis, and A. Mysyrowicz, Femtosecond Laser-Induced Damage and Filamentary Propagation in Fused Silica, Phys. Rev. Lett. **89**, 186601 (2002).

[44] S. Tzortzakis, L. Sudrie, M. Franco, B. Prade, A. Mysyrowicz, A. Couairon, and L. Bergé, Self-Guided Propagation of Ultrashort IR Laser Pulses in Fused Silica, Phys. Rev. Lett. **87**, 213902 (2001).

[45] W. J. Tropf and M. E. Thomas, *Handbook of Optical Constants of Solids* (Academic, New York, 1997).

[46] V. Jukna, J. Galinis, G. Tamosauskas, D. Majus, and A. Dubietis, Infrared extension of femtosecond supercontinuum generated by filamentation in solid-state media, Appl. Phys. B **116**, 477 (2014).

[47] A. A. Dergachev, V. Kadan, and S. Shlenov, Interaction of noncollinear femtosecond laser filaments in sapphire, Quantum Electron. **42**, 125 (2012).

[48] D. E. Zelmon, D. L. Small, and R. Page, Refractive-index measurements of undoped yttrium aluminum garnet from 0.4 to 5.0 μm, Appl. Opt. **37**, 4933 (1998).

[49] F. Silva, D. R. Austin, A. Thai, M. Baudisch, M. Hemmer, D. Faccio, A. Couairon, and J. Biegert, Multi-octave supercontinuum generation from mid-infrared filamentation in a bulk crystal, Nat. Commun. **3**, 807 (2012).

[50] K. V. Lvov, S. Y. Stremoukhov, E. A. Migal, and F. V. Potemkin, Asymmetric temporal splitting of laser pulse and broad supercontinuum generation under femtosecond filamentation in YAG crystal, Laser Phys. Lett. **15**, 085402 (2018).

[51] J. Galinis, G. Tamošauskas, I. Gražulevičiūtė, E. Keblytė, V. Jukna, and A. Dubietis, Filamentation and supercontinuum generation in solid-state dielectric media with picosecond laser pulses, Phys. Rev. A **92**, 033857 (2015).

[52] M. E. Thomas and W. J. Tropf, Optical properties of diamond, Johns Hopkins APL Tech. Dig. **14**, 16 (1993).

[53] K. Lee, B. J. Sussman, J. Nunn, V. Lorenz, K. Reim, D. Jaksch, I. Walmsley, P. Spizzirri, and S. Prawer, Comparing phonon dephasing lifetimes in diamond using transient coherent ultrafast phonon spectroscopy, Diam. Relat. Mater. **19**, 1289 (2010).

[54] R. Boyd, *Nonlinear Optics* (Academic, New York, 2008).

[55] T. M. Karda, B. Ratajska-Gadomska, W. Gadomski, A. Lapini, and R. Righini, The role of stimulated Raman scattering in supercontinuum generation in bulk diamond, Opt. Express **21**, 24201 (2013).

[56] P. Ščajev, V. Gudelis, E. Ivakin, and K. Jarašiūnas, Nonequilibrium carrier dynamics in bulk HPHT diamond at two-photon carrier generation, Phys. Status Solidi A **208**, 2067 (2011).

[57] Y.-H. Chuang, L. Zheng, and D. Meyerhofer, Propagation of light pulses in a chirped-pulse-amplification laser, IEEE J. Quantum Electron. **29**, 270 (1993).

[58] J. M. Dudley, G. Genty, and S. Coen, Supercontinuum generation in photonic crystal fiber, Rev. Mod. Phys. **78**, 1135 (2006).

[59] L. Mandel and E. Wolf, *Optical Coherence and Quantum Optics* (Cambridge University Press, Cambridge, England, 1995).

[60] R. Liao, C. Mei, Y. Song, A. Demircan, and G. Steinmeyer, Spontaneous emission noise in mode-locked lasers and frequency combs, Phys. Rev. A **102**, 013506 (2020).

[61] M. Rhodes, G. Steinmeyer, J. Ratner, and R. Trebino, Pulse-shape instabilities and their measurement, Laser Photon. Rev. **7**, 557 (2013).

[62] R. Trebino, R. Jafari, S. A. Akturk, P. Bowlan, Z. Guang, P. Zhu, E. Escoto, and G. Steinmeyer, Highly reliable measurement of ultrashort laser pulses, J. Appl. Phys. **128**, 171103 (2020).

[63] W. Koechner, Thermal lensing in a Nd:YAG laser rod, Appl. Opt. **9**, 2548 (1970).

[64] R. M. Sova, M. J. Linevsky, M. E. Thomas, and F. F. Mark, High-temperature infrared properties of sapphire, alon, fused silica, yttria, and spinel, Infrared Phys. Techn. **39**, 251 (1998).

[65] P. John, N. Polwarta, C. Troupea, and J. Wilson, The oxidation of (100) textured diamond, Diam. Relat. Mater. **11**, 861 (2002).

[66] I. H. Malitson, F. V. Murphy, and W. S. Rodney, Refractive index of synthetic sapphire, J. Opt. Soc. Am. **48**, 72 (1958).

[67] T. Ruf, M. Cardona, C. S. J. Pickles, and R. Sussmann, Temperature dependence of the refractive index of diamond up to 925 K, Phys. Rev. B **62**, 16578 (2000).

[68] M. Seal, Graphitization of diamond, Nature (London) **185**, 522 (1960).

[69] C. Brée, A. Demircan, and G. Steinmeyer, Method for computing the nonlinear refractive index via Keldysh theory, IEEE J. Quantum Electron. **46**, 433 (2010).

[70] S. Birkholz, E. T. J. Nibbering, C. Brée, S. Skupin, A. Demircan, G. Genty, and G. Steinmeyer, Spatiotemporal Rogue Events in Optical Multiple Filamentation, Phys. Rev. Lett. **111**, 243903 (2013).